Recovery of Negative and Positive Bias Temperature Stress in pMOSFETs

Ph. Hehenberger[*], H. Reisinger[°], and T. Grasser[•]

[*] Institute for Microelectronics, TU Wien, A-1040 Wien, Austria

[°] Infineon Technologies, D-81739 München, Germany

[•] Christian Doppler Laboratory for TCAD at the Institute for Microelectronics, TU Wien, A-1040 Wien, Austria

Abstract— **Based on the asymmetric recovery behavior observed following negative and positive bias temperature stress in pMOSFETs, various stress tests with different stress times, oxide electric fields, and oxide thicknesses were performed. In contrast to NBTI, where the relaxation of the threshold voltage often follows a logarithmic behavior, PBTI stress reveals no logarithmic recovery. Notable relaxation after PBTI stress instead appears to happen later but faster. This asymmetry is more pronounced at harsher stress conditions, e.g. increasing stress time and oxide electric field. This can be explained by the different relative measurement windows for NBTI and PBTI, which depend on the stress time and the oxide electric field. A closer analysis of the recovery yields the spectra of capture and emission time constants of the underlying defects. We analyze the dependence of these spectra on the stress time and the oxide electric field, where the emission times of the defects are shifted towards smaller times for higher oxide electric field.**

INTRODUCTION

Already decades ago the semiconductor industry discovered reliability issues such as the bias temperature instability (BTI), which happens when the gate of a heated metal-oxide-semiconductor field effect transistor (MOSFET) is biased while keeping the other contacts grounded [1, 2]. The degradation of device parameters, such as the threshold voltage V_{th} or the mobility, finally limits the operating lifetime of the transistor [3, 4]. This issue has become more important with decreasing device sizes and higher operation temperatures and has caused a considerable debate on the underlying physics and its consequences. Motivated by [5], the apparent differences in relaxation behavior of negative and positive BTI (NBTI and PBTI) on pMOSFETs are studied.

Although PBTI on pMOSFETs is technologically not as important as NBTI, it provides a valuable probe of the underlying physical degradation mechanism. The most intriguing observation is that both negative and positive bias stress create positive charges in the oxide [5]. While degradation built up during PBTI stress is about a factor two smaller than that built up during NBTI, up to medium stresses the degradation also recovers in a similar fashion. NBTI shows nearly perfect logarithmic relaxation when stressed up to $-6.5\,\text{MV/cm}$ for $100\,\text{ks}$, but deviations are found for higher stress fields ($E_{ox} = -8\,\text{MV/cm}$), depicted in the top of Fig. 1. It appears that the strong relaxation in the initial phase ranging from $1\,\mu\text{s}$ to about $100\,\text{ms}$ slows down to finally saturate. This saturation level is often called "permanent component" in contrast to the already recovered component [5, 6]. After [7] this permanent component follows a power-law. However, when comparing these two cases (low vs. high field) for PBTI, other effects become visible. Moderate PBTI stress ($6\,\text{MV/cm}$) yields a constant recovery rate per decade, comparable to the case of NBTI with $E_{ox} = 6\,\text{MV/cm}$. In contrast, for high-field PBTI stress the recovery is first delayed and then pronounced.

I. EXPERIMENTAL SETUP

NBTI/PBTI stress at $125\,^{\circ}\text{C}$ were performed using the fast-V_{th} method of [8]. PMOSFETS from a standard $90\,\text{nm}$ CMOS process with plasma-nitrided oxide (around $6\,\%$ of nitrogen) with
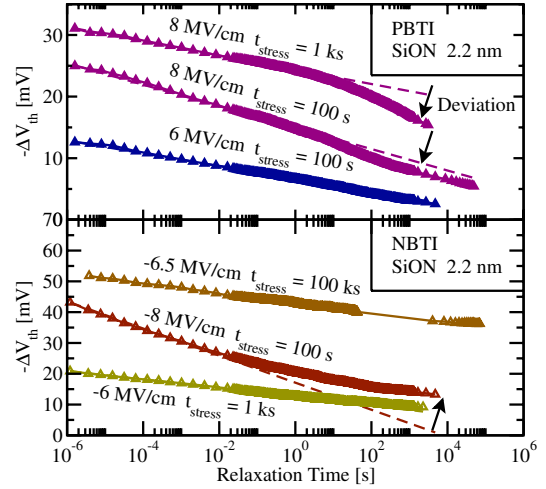

Fig. 1. Samples with an oxide thickness of $2.2\,\text{nm}$ stressed using various NBTI/PBTI-conditions from $100\,\text{s}$ up to $10\,\text{ks}$. Depending on the type of stress, there is either no deviation from a logarithmic recovery behavior, a deviation downwards (PBTI) or upwards (NBTI). While for weak NBTI/PBTI-conditions ($E_{ox} = \pm 6\,\text{MV/cm}$ and $t_{stress} = 100\,\text{s}$) a logarithmic fit of the relaxation is possible, this is not the case for the other heavier stress conditions.

three different oxide thicknesses ($t_{ox} = 1.8\,\text{nm}, 2.2\,\text{nm}$, and $5.0\,\text{nm}$) and geometries of $W/L = 20\,\mu\text{m}/0.12\,\mu\text{m}, 20\,\mu\text{m}/0.12\,\mu\text{m}$, and $20\,\mu\text{m}/0.24\,\mu\text{m}$, respectively, were used.

II. SCHEMATIC RECOVERY BEHAVIOR

In order to be able to discuss our experimental results we summarize our key findings first. The complete recovery trace after BTI stress is schematically depicted in the top left of Fig. 2. Unfortunately, the full features are rarely visible, compare with the curve of $E_{ox} = -8\,\text{MV/cm}$ and $t_{stress} = 100\,\text{s}$ in Fig. 1.

Actually, the monitored relaxation characteristics after typical BTI stress is limited in range. While for PBTI only the upper section of the whole relaxation curve is visible, it is the lower section for NBTI. Within these sections τ_A and τ_B depend on the curvatures and mark the transition between the initial and the late phase of the recovery. Using the curvature to detect a change of the relaxation we will analyze the recovery following PBTI versus NBTI stress.

III. EXTRACTION ROUTINE

The determination of the curvature following bias temperature stress is displayed in Fig. 3. First, each relaxation of V_{th} is referred to its initial $V_{th,0}$ and is plotted as ΔV_{th} as a function of $\log(t)$. The first decades as well as the last decade in time are used to fit the experimental data with a logarithm of the form $a + b\log(t)$, giving the initial and long term recovery behavior. Eventually, the intersection of the two fits results in the "kink point" τ_A or τ_B.
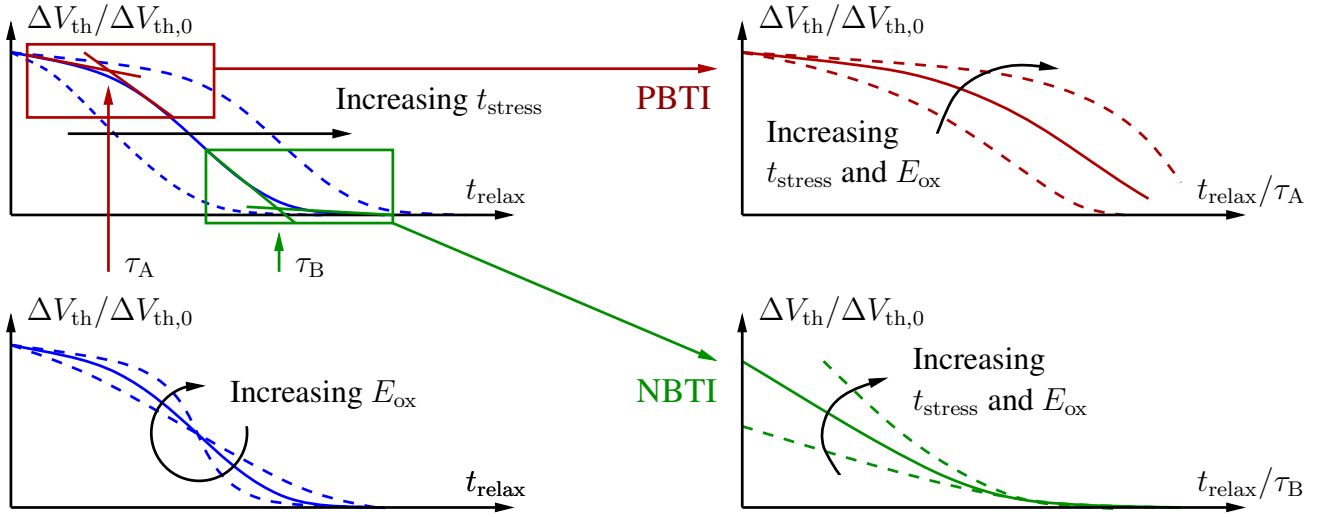
Fig. 2. A schematic recovery trace after bias temperature stress is shown as solid line. **TopLeft**: The full S-shape is only observable under certain conditions, e.g. $E_{ox} = -8\,\mathrm{MV/cm}$ and $t_{stress} = 100\,\mathrm{s}$. For longer t_{stress} the whole curve is shifted to higher t_{relax}. PBTI mainly shows the characteristics in the top left (red) box, whereas the behavior after NBTI stress typically proceeds as shown in the bottom right (green) box. Within these sections τ_A and τ_B depend on the curvatures and mark the transition between the initial and the concluding phase of the recovery. **BottomLeft**: In combination with the oxide electric field dependence, the behavior of PBTI and NBTI can be obtained by scaling with τ_A and τ_B. **TopRight**: Increasing stress conditions (t_{stress} and/or E_{ox}) for PBTI yields smaller relaxation rates per decade at earlier t_{relax}/τ_A, followed by larger relaxation rates afterwards. When extending the observation period towards larger t_{relax}/τ_A, the transition back to smaller relaxation rates becomes visible. **BottomRight**: Increased stress conditions after NBTI feature increased relaxation up to τ_B. Extending the observation period towards smaller t_{relax}/τ_B after NBTI stress is more difficult due to the limited measurement speed.
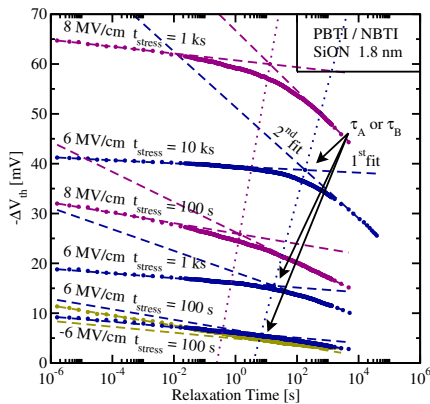

Fig. 3. The relaxation behavior starts to deviate from the logarithmic shape at harsher stress conditions. By fitting the beginning and the end of the recovery traces separately, a kink point τ_A or τ_B at the extrapolated intersection of the fits can be obtained, which characterizes the curvature. Comparing kink points of the same electric field and oxide thickness for different stress times (connected by dotted lines) shows that this curvature is stronger at longer stress times and delayed with time.
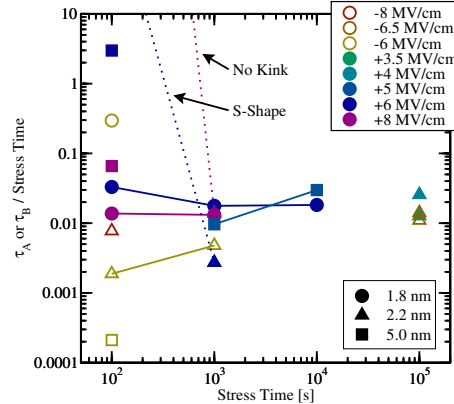
Fig. 4. As already shown by the dotted lines in Fig. 3, a longer stress increases the kink time τ_A for PBTI or τ_B for NBTI. Scaling τ_A or τ_B to t_{stress} reveals a proportionality of the kink time and t_{stress}. The extraction does not work properly with two kinks at τ_A and τ_B or without a kink, due to the glancing intersection of the fits, resulting in an ambiguous kink point. The positions for these special cases at $t_{stress} = 100\,\mathrm{s}$ are indicated by dotted lines.
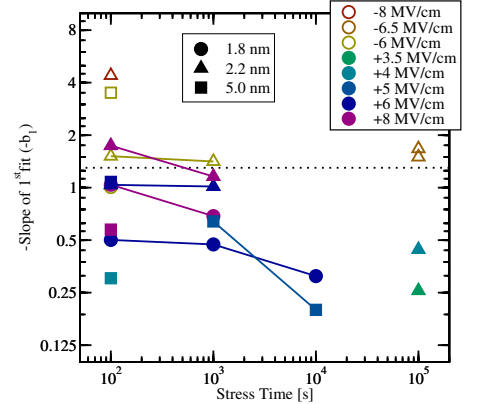
Fig. 5. The slope b_1 of NBTI-stress is higher than that resulting from PBTI-stress, and it is decreasing with t_{stress} as shown by the solid lines. The dashed line denotes the barrier of NBTI and PBTI, very close to 1. The initial relaxation slopes b_1 are spread from 0.196 (PBTI) to 4.35 (NBTI), which is a factor of more than 20. This demonstrates the different initial relaxation behavior following NBTI and PBTI stress.

However, the kink-point-method does not work properly with too similar logarithmic prefactors b_1 and b_2 due to glancing intersection (compare $E_{ox} = \pm 6\,\mathrm{MV/cm}$ and $t_{stress} = 100\,\mathrm{s}$ in Fig. 3). For the already discussed complete recovery trace with its S-shape, the first and second fit become nearly parallel resulting in an undetermined kink point.

IV. EXPERIMENTAL OUTPUT

The curvature due to different kind of stress with varying t_{stress} and E_{ox} will now be evaluated using different oxide thicknesses. Its origin is described on the basis of Fig. 3 for the $1.8\,\mathrm{nm}$ thick oxides

and can be split up into a stress time component and an oxide field component.

First, the position of the curvature, characterized by τ_A or τ_B, obviously depends on the stress conditions, which is displayed in Fig. 4 in more detail. The longer the device is stressed for equal E_{ox}, the later the kink occurs. Normalizing the kink-time to the stress time t_{stress} yields a constant, indicating a connection between t_{stress} and the recovery behavior. This is schematically shown in Fig. 2, where increasing t_{stress} shifts the relaxation curve towards larger t_{relax}. Additionally, the associated shift towards higher initial $\Delta V_{th,0}$ vanishes, when the relaxation is scaled.
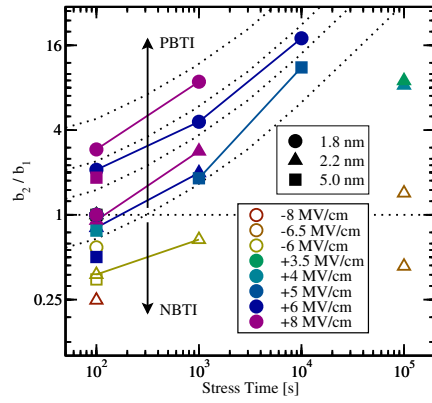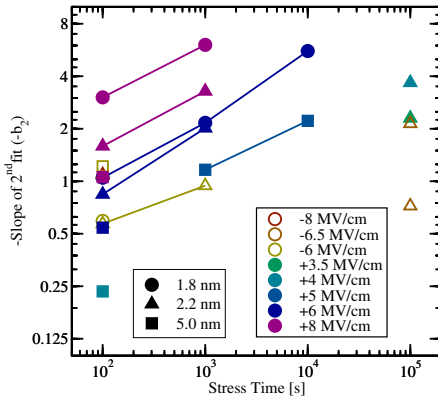
Fig. 6. **Left**: The slope b_2 for the long-term characteristics is increasing with t_{stress} and E_{ox} and clearly depicts the increased relaxation after PBTI stress with values ranging from 0.53 (NBTI) to 5.99 (PBTI). This and the fact that PBTI nearly does not recover the first few seconds hold for longer emission times but not until harsher stress conditions. **Right**: The ratio b_2/b_1 increases with increasing t_{stress} and E_{ox} ranging from NBTI with $-8\,\mathrm{MV/cm}$ up to PBTI with $+8\,\mathrm{MV/cm}$. NBTI-stressed samples with a negative kink feature a ratio smaller or equal to 1, whereas PBTI-stressed ones possess values from 1 up to 20. Higher ratios are restricted by the maximum allowed electric field E_{ox} before the oxide breaks down.

Fig. 7. Using only a single slope for the recovery characterization cancels the visible effect of E_{ox} as it manifests with t_{relax}. Hence, the geometric mean of b_1 and b_2 is nearly constant for all analyzed devices despite its weak t_{stress}-dependence. This implies that the evaluation of a single slope is not valid for heavier stress conditions because of the asymmetric and limited observation period.

V. Short-Term and Long-Term Relaxation

To be able to discuss the effect of E_{ox} on the relaxation we again have to refer to Fig. 3. When comparing the devices stressed for 1 ks with 6 MV/cm and 8 MV/cm, τ_A has approximately the same value, but the relative relaxation with respect to its very different $\Delta V_{th,0}$ changes as depicted in Fig. 2 bottom left. With a raise in the oxide electric field the recovery sets in late, but proceeds faster.

The slopes of the first (b_1) and second (b_2) logarithm, i.e. the short-term and long-term relaxation behavior can be explained using Fig. 5 and Fig. 6 left: (i) The initial relaxation b_1 after NBTI stress is higher than its PBTI counterpart. (ii) For NBTI, b_1 is increasing with increasing E_{ox}. (iii) For PBTI, b_1 is only slightly increasing with increasing E_{ox}. Due to also higher $\Delta V_{th,0}$ with higher E_{ox}, the effect even results in lower relative recovery per decade with higher E_{ox}. (iv) For PBTI, b_1 decreases with increasing t_{stress}.

The long-term relaxation b_2 increases with t_{stress} and E_{ox}, which clearly shows enhanced relaxation after PBTI-stress, but lower relaxation after NBTI compared to the corresponding b_1. All these results support the trends stated in Fig. 2.

By plotting the ratio b_2/b_1, one is able to specify the oxide electric field during the stress. In Fig. 6 right equal E_{ox} conditions at various t_{stress} values are connected for better visibility. Different E_{ox} values ranging from NBTI with $-8\,\mathrm{MV/cm}$ up to PBTI with $+8\,\mathrm{MV/cm}$ result in gradually increasing b_2/b_1. Despite some minor deviations for different device thicknesses this decomposes the prior performed kind of stress in a good manner. Samples stressed with NBTI feature a b_2/b_1 smaller or equal to 1. PBTI-stress, on the other hand, shows ratios from 1 up to 20. Hence, the ratio b_2/b_1 gives a measure of the symmetricity of the relaxation curve. This ratio indicates which section of the relaxation transient the original experiment recorded. If $b_2/b_1 < 1$, the experiment probed the second half of the S-shape, i.e. the long term relaxation, which is usually the case after NBTI. If $b_2/b_1 \approx 1$, the "main" part of the relaxation was monitored and both the initial as well as the late relaxation phase at least contribute to the total recovery to about the same degree.

Modeling the recovery with a single slope, which would then be approximately equal to the geometric mean of b_1 and b_2, clearly obscures the fact that the oxide electric field has an impact not only on the slope, but on the shape of the recovery as well. As depicted in Fig. 7, it is thus only possible to explain the t_{stress}-dependence.
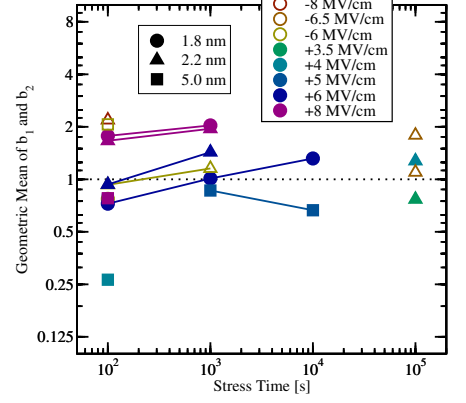
Moreover, the geometric mean requires symmetricity of the recovery trace, which is only given under moderate stress conditions.

Our results underline the fact that the changes of the recovery behavior with varying E_{ox} and t_{stress} are due to a change in the emission time rates of the defects [9–13], which will be discussed in detail in the next section.
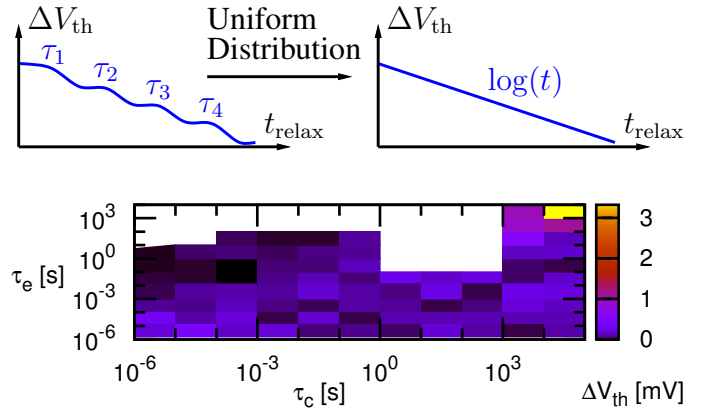

Fig. 8. **Top**: If there are few defects with emission times τ_i like in small-area transistors [13, 14], the relaxation after BTI exhibits discrete humps. Enlarging the area (more defects) and assuming a uniform distribution of them adds up to a $\log(t)$ behavior, instead. **Bottom**: Map of ranges of time constants of capture and emission.

VI. Emission Time Constants

Transistors with only a few defects relax in discrete steps at the defects' emission times $\tau_{e,i} = \tau_0 \exp(E_{A,i}/k_B T)$, which is clearly visible in small area devices [13, 14]. Larger devices contain a larger number of defects. This in combination with a uniform distribution of the activation energies $E_{A,i}$ yields a log-like recovery behavior as displayed in the top of Fig. 8. As there are many different $\tau_{c,i}$ and corresponding $\tau_{e,i}$ within the device, their extraction from the experimental data is discussed first.

By subtracting two recovery traces after stress times $t_{s,i}$ and $t_{s,i+1}$, the fraction of defects with capture time constants with
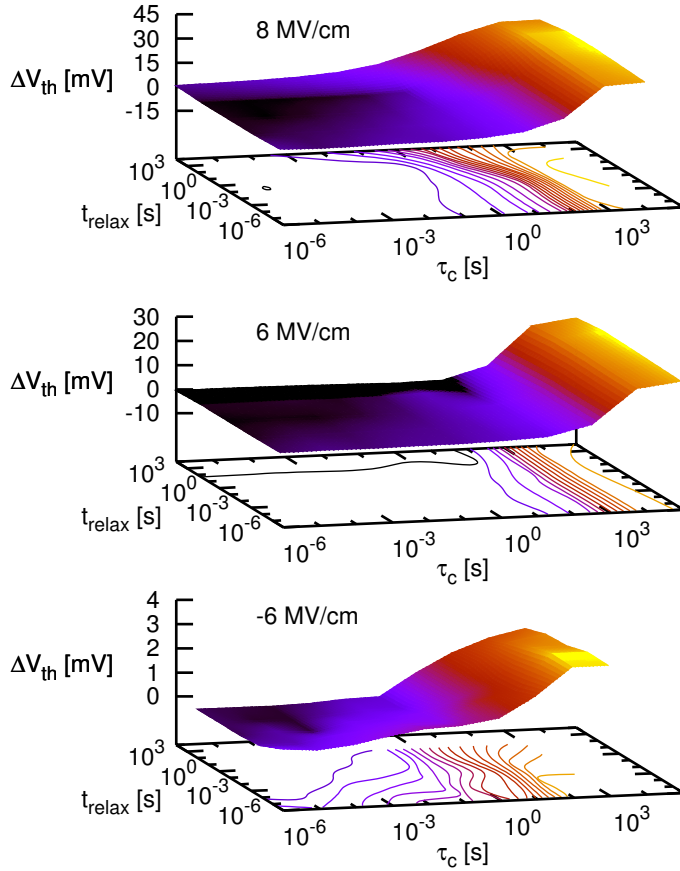
Fig. 9. The fraction of defects having $t_{s,i} < \tau_c < t_{s,i+1}$ and $t_{r,i} < \tau_e < t_{r,i+1}$ is depicted for three different oxide electric fields, with the contour lines below the graphs showing the biggest changes of ΔV_{th}. Both surface and contour lines are smoothed for a better visualization. It is shown that the oxide electric field is related to the amplitude of τ_e. Increasing E_{ox} yields a shift of the peak towards smaller τ_e, which corresponds to our monitored increased recovery at larger t_{relax}.

$t_{s,i} < \tau_c < t_{s,i+1}$ is determined [15]. By dividing the difference trace into intervals $[t_{r,i}, t_{r,i+1}]$, the fraction of defects having $t_{s,i} < \tau_c < t_{s,i+1}$ and $t_{r,i} < \tau_e < t_{r,i+1}$ is obtained.

To be able to describe the frequency of occurrence of capture time constants τ_c and emission time constants τ_e properly, a large set of long recovery traces with varying t_{stress} is needed. Our experiments cover τ_c from 10^{-6} s up to 10^4 s and τ_e intervals between 10^{-6} s and 10^3 s. This allows for extracting time constants as exemplarily depicted in the bottom of Fig. 8.

We are now able to explain the above mentioned effect with the varying oxide electric field on the basis of Fig. 9, where the fraction of ΔV_{th} due to defects with τ_c and τ_e is plotted as smoothed surface over τ_c and τ_e.

For NBTI with an E_{ox} of -6 MV/cm the surface shows two peaks. One peak covers τ_c and τ_e smaller than $1\,\mu$s, while the other more pronounced one clearly illustrates that the largest part of the degradation was due to defects with τ_c larger than 1 s, which is highlighted by the contour lines below the graph. When comparing the different E_{ox} for PBTI for τ_c covering time constants between 10^2 s and 10^3 s, the peak of 6 MV/cm mainly consists of $\tau_e > 10$ s, while it is widened for 8 MV/cm towards smaller τ_e. This supports our hypothesis of decreased τ_e for higher E_{ox} after PBTI stress, which is visualized by the faster long-term recovery.

VII. Conclusion

The relaxation behavior of stressed pMOSFETs depends on the field and stress time of the performed stress. Especially when dealing with PBTI, the harsher the conditions of stress the later the device starts to relax significantly. Using the limited observation period for NBTI and PBTI as part of the full recovery shape we are able to explain our experimental findings. The full features of the recovery curve can only be identified after moderate BTI stress, where the relaxation after a certain time accelerates, and slows down again later on. Furthermore, deeper analysis of the relaxation characteristics is a means to get information on the distribution of capture times and emission times of the defects assumed responsible for BTI. Higher oxide electric fields lead to emission times shifted towards smaller values.

References

[1] V. Huard, M. Denais, and C. Parthasarathy, "NBTI Degradation: From Physical Mechanisms to Modelling," *Microelectronics Reliability*, vol. 46, no. 1, pp. 1–23, 2006.

[2] D.K. Schroder and J.A. Babcock, "Negative Bias Temperature Instability: Road to Cross in Deep Submicron Silicon Semiconductor Manufacturing," *J. Appl. Phys.*, vol. 94, no. 1, pp. 1–18, Jul. 2003.

[3] J.H. Stathis and S. Zafar, "The Negative Bias Temperature Instability in MOS Devices: A Review," *Microelectronics Reliability*, vol. 46, no. 2-4, pp. 270, 2006.

[4] V. Reddy, A. T. Krishnan, A. Marshall, J. Rodriguez, S. Natarajan, T. Rost, and S. Krishnan, "Impact of Negative Bias Temperature Instability on Digital Circuit Reliability," in *Proc. Intl.Rel.Phys.Symp.*, 2002, pp. 248–254.

[5] T. Grasser, B. Kaczer, P. Hehenberger, W. Gös, R. O'Connor, H. Reisinger, W. Gustin, and C. Schlünder, "Simultaneous Extraction of Recoverable and Permanent Components Contributing to Bias-Temperature Instability," in *Proc. Intl.Electron Devices Meeting*, 2007.

[6] T. Grasser and B. Kaczer, "Negative Bias Temperature Instability: Recoverable versus Permanent Degradation," in *ESSDERC*, 2007, pp. 127–130.

[7] Ph. Hehenberger, P.-J. Wagner, H. Reisinger, and T. Grasser, "Comparison of Fast Measurement Methods for Short-Term Negative Bias Temperature Stress and Relaxation," in *ESSDERC*, 2009.

[8] H. Reisinger, O. Blank, W. Heinrigs, W. Gustin, and C. Schlünder, "A Comparison of Very Fast to Very Slow Components in Degradation and Recovery due to NBTI and Bulk Hole Trapping to Existing Physical Models," *T-DMR*, vol. 7, no. 1, pp. 119–129, Mar. 2007.

[9] V. Huard, C.R. Parthasarathy, and M. Denais, "Single-Hole Detrapping Events in pMOSFETs NBTI Degradation," in *IIRW*, 2005, p. 5.

[10] B. Kaczer, T. Grasser, J. Martin Martinez, E. Simoen, M. Aoulaiche, Ph. J. Roussel, and G. Groeseneken, "NBTI from the Perspective of Defect States with Widely Distributed Time Scales," in *Proc. Intl.Rel.Phys.Symp.*, 2009, pp. 55–60.

[11] H. Reisinger, T. Grasser, and C. Schlünder, "A Study of NBTI by the Statistical Analysis of the Properties of Individual Defects in pMOSFETs," in *IIRW*, 2009, pp. 60–63.

[12] B. Kaczer, T. Grasser, Ph. J. Roussel, J. Franco, R. Degraeve, L.-A. Ragnarsson, E. Simoen, G. Groeseneken, and H. Reisinger, "Origin of NBTI Variability in Deeply Scaled pFETs," in *Proc. Intl.Rel.Phys.Symp.*, 2010.

[13] T. Grasser, H. Reisinger, W. W. Gös, Th. Aichinger, Ph. Hehenberger, P.-J. Wagner, M. Nelhiebel, J. Franco, and B. Kaczer, "Switching Oxide Traps as the Missing Link Between Negative Bias Temperature Instability and Random Telegraph Noise," in *Proc. Intl.Electron Devices Meeting*, 2009.

[14] T. Grasser, H. Reisinger, P.-J. Wagner, F. Schanovsky, W. Gös, and B. Kaczer, "The Time Dependent Defect Spectroscopy (TDDS) for the Characterization of the Bias Temperature Instability," in *Proc. Intl.Rel.Phys.Symp.*, 2010.

[15] H. Reisinger, T. Grasser, W. Gustin, and C. Schlünder, "The Statistical Analysis of Individual Defects Constituting NBTI and its Implications for Modeling DC- and AC-Stress," in *Proc. Intl.Rel.Phys.Symp.*, 2010.